A macro-element pile foundation model for integrated analyses of monopile-based offshore wind turbines

Ana M. Page[a,b], Gustav Grimstad[a], Gudmund Reidar Eiksund[a], Hans Petter Jostad[a,b]

[a] *Norwegian University of Science and Technology (NTNU), Trondheim, Norway*
[b] *Norwegian Geotechnical Institute (NGI), Oslo, Norway*

Abstract

The design of OWTs relies on integrated load analyses tools that simulate the response of the entire OWT (including the rotor-nacelle assembly, support structure and foundation) under combined aerodynamic and hydrodynamic loading. Despite all efforts to develop accurate integrated models, these often fail to reproduce the measured natural frequencies, partly due to the current foundation modelling. This paper presents a new foundation model for integrated analyses of monopile-based OWTs. The model follows the macro-element approach, where the response of a pile and the surrounding soil is condensed to a force-displacement relation at seabed. The model formulation uses multi-surface plasticity and it reproduces key characteristics in monopile foundation behaviour that are not accounted for in current industry practice. The basic features of the model are described and its limitations are discussed. The performance of the macro-element model is compared against field test measurements and results from FEA. The comparison indicates that the macro-element model can reproduce accurately the non-linear load-displacement response and hysteretic behaviour measured in field tests and computed in FEA. This confirms that the model can simulate the pile and soil behaviour with the same level of accuracy as FEA, but with a considerable reduction in computational effort.

Keywords: Offshore Wind Turbine, Pile Foundation, Soil-Structure Interaction, Foundation Damping, Load Calculation Methods, Macro-element Model

1. Introduction

Designing offshore wind turbines is a complex task as these are dynamic systems subjected to variable cyclic loads. Fatigue often drives the design, and therefore dynamic structural analyses are mandatory (Det Norske Veritas, 2014). Dynamic structural analyses are based on integrated load simulations of several design load cases (Vorpahl et al., 2013), and they are generally performed in the time-domain (Det Norske Veritas, 2014). An integrated analysis of an OWT refers to the analysis of an entire OWT (i.e. rotor-nacelle-assembly, support structure, and foundation) under combined aerodynamic and hydrodynamic loading and requires numerical models for all parts of the OWT (see Fig. 1). The foundation model is an essential part of the integrated model due to its impact on the fatigue (Aasen et al., 2017). Among the different concepts for OWT support structures, the monopile is the preferred solution, accounting for approximately 80% of the installed support structures (Wind Europe, 2018).

For monopile-based OWTs, the current industry design practice is to model the foundation response by API p-y curves (Det Norske Veritas, 2014, American Petroleum Institute, 2014). The API p-y curve methodology has been successfully applied for pile design in the oil and gas industry for many decades (Arshad and O'Kelly, 2016). However, discrepancies between the response obtained with the API formulation and the actual monopile behaviour have been extensively identified in the literature (Lesny, 2010, Doherty and Gavin, 2011), and their applicability to predict pile behaviour in integrated analyses of OWTs has been questioned. In addition to these shortcomings, comparison between designed and

measured fundamental frequencies from monopile-based OWTs reveals that the fundamental frequencies are generally underestimated in the design (Zaaijer, 2006, Kallehave, Byrne, Thilsted and Mikkelsen, 2015). Zaaijer (2006) and Kallehave, Thilsted and Troya (2015) indicated that this is consistent with the notion that the API p-y curve formulation for piles in sand tends to underestimate the soil stiffness. Hald et al. (2009) brought into comparison the measured and the predicted bending moments using API $p-y$ curves for a pile in sand at the Horns Rev wind farm; and also concluded that the soil response was underestimated by the API $p-y$ curves. Moreover, API p-y curves are generally modelled as non-linear elastic, and cannot reproduce the foundation damping measured in OWTs (Tarp-Johansen et al., 2009, De Vries et al., 2011, Shirzadeh et al., 2013, Damgaard et al., 2013).

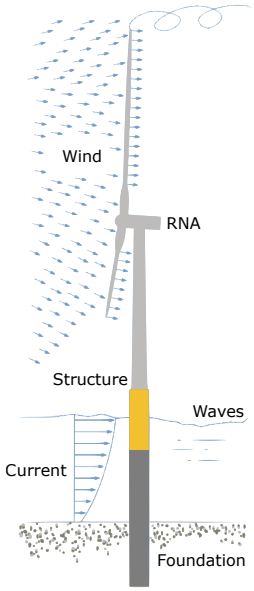

Figure 1: Environmental actions on a monopile-based offshore wind turbine.

Given the limitations of the API p-y curves, some first steps have been taken to improve the foundation modelling (Byrne et al., 2015, Shadlou and Bhattacharya, 2016, Hededal and Klinkvort, 2010, Damgaard et al., 2014, Beuckelaers, 2015, Beuckelaers et al., 2017). These models have either focused on improving the foundation stiffness response (Byrne et al., 2015, Shadlou and Bhattacharya, 2016) or the modelling of foundation damping (Hededal and Klinkvort, 2010, Damgaard et al., 2014, Beuckelaers, 2015). However, there is still a lack of models that can provide simultaneously accurate foundation stiffness and damping in integrated time-domain simulations of monopile-based OWTs.

An alternative modelling approach that can provide both accurate foundation stiffness and damping is macro-element modelling. Macro-element models condense the response of the foundation and the surrounding soil to a force-displacement relation at one point separating the foundation and the rest of the structure, typically located at seabed (Correia, 2011). The response at this point can be determined from numerical analyses of the pile and soil, for instance from Finite Element Analyses (FEA), or from model testing. Modelling pile foundations with macro element models has some advantages compared to the $p-y$ curve approach. First, the contribution of some components of soil resistance such as side and base shear, which might be relevant for monopile-based OWTs, are not included in the traditional $p-y$ methodology, but are included in the macro-element model. Second, the response of the foundation is only computed in one node, which means that fewer degrees of freedom are required in integrated analyses than for distributed $p-y$ curves. Finally, in layered soils it is easier to accurately describe the overall stiffness and hysteretic damping response at seabed than accurately describing the varying $p-y$

stiffness and damping response along the length of the pile.

The macro-element concept has been succesfully applied to describe the behaviour of shallow foundations in offshore applications, such as jack-up spudcan foundations (Houlsby and Cassidy, 2002, Bienen et al., 2006), pipelines (Tian and Cassidy, 2008), skirted foundations supporting OWTs (Skau et al., 2017), or anchor-block foundations for bridges installed in deep waters (Tistel et al., 2017). The concept has also been employed to model the response of shallow (Cremer et al., 2001) and deep foundations (Correia, 2011, Li et al., 2016) in time-domain simulations of earthquake events. These pile macro-element models can reproduce the non-linear hysteretic load-displacement response observed in piles, however, they also accumulate displacements after a few loading cycles. Significant accumulated displacements are not expected for the relatively low load levels and for the number of cycles present in the 10 to 60 minutes long time windows considered in integrated load simulations of OWTs, and therefore these models are not directly applicable. Despite the potential to provide accurate foundation stiffness and damping, the macro-element approach has rarely been employed in integrated analyses of monopile-based OWTs (Krathe and Kaynia, 2017, Page et al., 2017).

In this paper, a new macro-element model for cyclic undrained loading of piles is presented. The model aims at predicting the load-displacement response and the hysteretic damping of piles in integrated time-domain analyses of monopile-based OWTs. The model formulation is based on multi-surface plasticity (Iwan, 1967), and it represents a new application of this framework. The paper is structured as follows. Section 2 presents the 3D FEA of the pile and the surrounding soil volume used as a basis for the model formulation. Then, Section 3 describes the macro-element formulation, implementation and calibration. After this, Section 4 illustrates the performance of the macro-element model and compares it against FEA and field tests. Finally, Section 5 lists the model limitations and Section 6 outlines the conclusions.

2. Numerical database

2.1. Introduction

Finite Element Analyses (FEA) of the soil volume and the foundation are performed to set the basis of the macro-element model. The FEA simulate the layered soil conditions and pile dimensions found in a real wind farm (Hamre et al., 2010, Le et al., 2014). A numerical approach was selected over physical model testing because model tests are generally costly and relatively few loading paths can be considered. In addition, it is difficult to reproduce the layered soil conditions often found in offshore wind farms in experimental set-ups, especially when it involves clay (Cremer et al., 2001).

2.2. System definitions

Modelling the foundation behaviour in integrated analyses of offshore wind turbines involves defining the foundation response along six degrees of freedom (three displacements: u_x, u_y, u_z, and three rotations: $\theta_x, \theta_y, \theta_z$). In the foundation model described in this paper, the response along the six degrees of freedom is included as follows. The responses to vertical (u_y) and torsional (θ_z) loading are modelled elastic and uncoupled. The response to lateral loading ($u_x - \theta_y$ and $u_y - \theta_x$) is described as non-linear and the coupling between the horizontal displacement at the rotation is accounted for. Despite the foundation model does not include all possible interactions between the six degrees of freedom, it accounts for the interaction between the most important loads acting on a pile supporting a monopile-based OWT subjected to a main wind direction.

In the following sections, focus is set on describing the response to planar lateral loading. Consequently, when analysing the pile-foundation system, it is assumed that the pile head is subjected to a

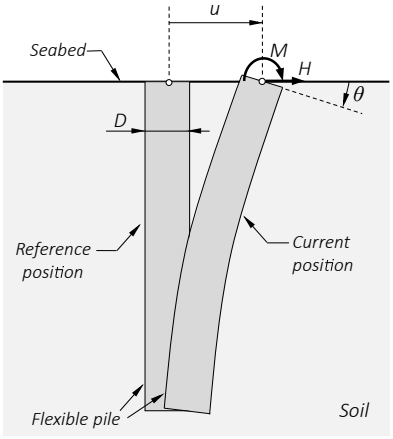

Figure 2: Loads and corresponding displacement components in the vertical plane of symmetry. Sign convections according to Butterfield et al. (1997)

two-dimensional loading system, composed by a horizontal load H, and an overturning moment M orthogonal to the direction of the horizontal load. The loads are applied at the centre of the cross-section of the pile. In this manner, the deformations of the pile axis, the horizontal displacement u and rotation θ at the pile head are contained in the vertical plane defined by H. Fig. 2 presents the notation for the pile head loads and displacements, together with the sign convection suggested by Butterfield et al. (1997). It might also be convenient to write the loads M and H as a generalised load vector $\boldsymbol{t}$, and the displacements (θ, u) as the work conjugate generalised displacement vector $\boldsymbol{v}$, as described by Eq. 1.

$$\boldsymbol{t} = \begin{bmatrix} \frac{M}{D} \\ H \end{bmatrix}; \quad \boldsymbol{v} = \begin{bmatrix} D \cdot \theta \\ u \end{bmatrix} \tag{1}$$

2.3. Numerical model

This section describes the foundation geometry, soil conditions and numerical model of the reference case used to characterise the pile-foundation lateral behaviour. The reference case is based on one of the monopiles at the Sheringham Shoal wind farm located in the North Sea off the coast of Norfolk. The Sheringham Shoal wind farm accommodates 88 monopile-based offshore wind turbines installed in water depths varying between 15 and 23 m. The monopiles have diameters ranging from 4.7 to 5.7 m, penetrating in the soil between 23 and 37 m (Hamre et al., 2010). Arany et al. (2017) report pile wall thickness in the order of 0.06 m.

The soil conditions at Sheringham Shoal consist of four main soil units: the Bolders Bank clay, the Egmond Ground sand, the Swarte Bank clay and the Chalk rock. The Bolders Bank Formation is a firm to stiff clay with pockets of sands, gravels and occasionally boulders. The Egmond Ground formation, which comprises dense to very dense sand, overlies the Swarte Bank formation, which is composed of stiff to hard sandy-gravelly clay. Underneath, several levels of Chalk are present. These four units extend over large areas in the southern part of the North Sea (Le et al., 2014) and therefore it is feasible to find them at other wind farms in the vicinity. Consequently, these conditions are more representative for piles supporting OWT than idealized soil profiles often used in model development. More details of the geological and geotechnical characterisation of these soil units are described in Le et al. (2014).

In the reference case, a steel pile with a diameter of 5.7 m and a wall thickness of 0.06 m, penetrating 28.5 m into the soil is considered. Three of the main soil layers: the Bolders Bank clay, the Egmond Ground sand, and the Swarte Bank clay are included. Maximum shear modulus and undrained shear strengths (from UU and CAU) measurements for these layers are plotted in Fig. 3. The pile is considered

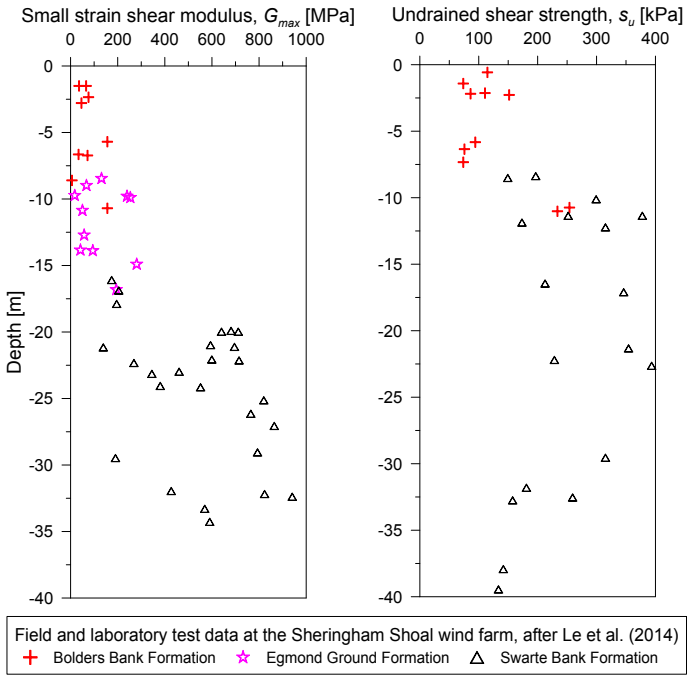

Figure 3: Small strain shear modulus (G_{max}) and undrained shear strength (s_u) with depth from laboratory tests, modified after Le et al. (2014).

linear elastic, and its behaviour is described by a Young's modulus of 210 GPa; while the soil units are modelled by elasto-plastic models. The behaviour of the clay layers in the numerical model is represented by the NGI-ADP soil model (Grimstad et al., 2012), which describes the elasto-plastic, non-linear stress path dependent behaviour of saturated clays under undrained monotonic loading conditions. A shear stress-strain curve interpreted from direct simple shear (DSS) laboratory tests is compared in Fig. 4 with the NGI-ADP soil model for the Bolders Bank soil layer. Good agreement is found from small to large strain levels. The available experimental data is insufficient for assessing the effect of soil anisotropy on the clay strength and stiffness, and consequently the clay is modelled as an isotropic material. The sand is represented in the numerical model as undrained with the Hardening Soil Small Strain model (Benz, 2007), a model developed to describe the behaviour of sands from small-strains to large strains. The parameters employed to describe the soil units behaviour are listed in Table 1. The contact between the soil and the pile is modelled by interface elements. The stiffness of the interface is equivalent to the soil stiffness, while the interface strength in compression is half of the soil strength. The interface strength in extension is governed by a no-tension criterion that allows gap opening between the soil and the pile.

The commercial software PLAXIS 3D (Brinkgreve et al., 2015) is employed to perform the three-dimensional FEA. Both the problem geometry and the loading are symmetric around the vertical plane defined by H, therefore, it is sufficient to include half of the geometry and the loads in the numerical model. Fig. 5 shows the mesh discretization, together with the model dimensions. The mesh has 230 000 10-noded tetrahedral soil elements with an average element side length of 2 m. The mesh is refined around the pile, where an average element side length of 0.6 m is used. The pile is modelled as a solid volume with an equivalent stiffness that reproduces the bending stiffness of the hollow pile, neglecting the stiffness of the soil plug. Pile installation effects are not considered, and the pile is modelled as 'wished in place' in initially undisturbed ground conditions.

Boundary conditions are applied at the base of the model and at the vertical boundaries. The three

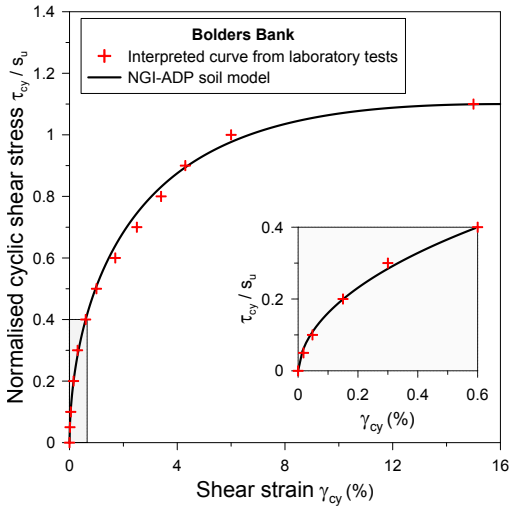

Figure 4: Comparison of the NGI-ADP model prediction with the non-degraded cyclic shear stress-strain relationship interpreted from DSS laboratory tests of the Bolders Bank soil unit at Sheringham Shoal.

displacements components in the three coordinate directions are set to zero at bottom boundary. On the vertical boundaries, the normal component is fixed. In the simulations, different combinations of H and M are applied at the pile head's cross-section (see Fig. 2) in a load-controlled manner, following a radial path in the load plane defined by H and M.

2.4. Simulated pile-foundation behaviour

The response of the pile-foundation and the surrounding soil to different load combinations is evaluated by analysing the computed displacements of the pile head at seabed. Fig. 6 shows the computed elasto-plastic horizontal displacement u and rotation $D \cdot \theta$, together with an interpolated surface. To ease the visualization of results and the formulation of the model, the elasto-plastic response is divided into an elastic and a plastic part. As expected, the flat shape of the interpolated elastic response indicates that the elastic rotation $D \cdot \theta^e$ and the elastic horizontal displacement u^e can be expressed as a linear relation between M/D and H, for instance through an elastic stiffness matrix.

The relation between the plastic rotation $D \cdot \theta^p$ and the plastic horizontal displacement u^p at seabed and the loads M/D and H is non-linear and makes the elasto-plastic surface in Fig. 6 curved. While trying to analyse how the plastic displacements are generated as a function of the loads, it might be convenient to look at how the plastic work evolves. For a radial load path with loads $(M/D, H)$, where the plastic displacements $(D \cdot \theta^p, u^p)$ are generated, the plastic work W^p can be calculated as:

$$W^p = \int_0^{\theta^p} M \cdot d\theta^p + \int_0^{u^p} H \cdot du^p \tag{2}$$

The plastic work computed from the Sheringham Shoal reference case analyses is shown in Fig. 7 as contours in the $(M/D, H)$ plane. Along these contours, the plastic work generated is constant. The shape of the contours can be approximated by an ellipse, as illustrated in Fig. 7a. In addition, Fig. 7b plots the direction of the computed incremental plastic displacement vectors $(D \cdot d\theta^p, du^p)$, which are perpendicular to the plastic work contours. This is convenient as the direction of the incremental plastic displacement vectors could be expressed as the gradient of the plastic work contours, simplifying the macro-element model formulation. Based on these findings, a macro-element model for piles that relates the loads $(M/D, H)$ and the pile head displacements $(D \cdot \theta, u)$ at seabed is proposed.

Table 1: Model parameters for the soil units at Sheringham Shoal.

	Bolders Bank	**Egmond Ground**	**Swarte Bank**
Unit Weight, γ (kN/m^3)	21.3[(1)]	20.3[(1)]	21.3[(1)]
Plasticity index, IP (%)	30[(1)]	-	15[(1)]
Undrained shear strength, s_u (kPa)	10-150	-	195-325
Ratio between the shear modulus at very small strains and s_u, G_{max}/s_u $(-)$	1200	-	800-2400
Shear srain at failure, γ_f (%)	16[(2)]	-	20[(2)]
Relative density, D_r (%)	-	80-100[(1)]	-
Drained friction angle, ϕ (°)	-	48.5[(1)]	-
Dilatancy angle, ψ (°)	-	18.5	-
Power for stress-level dependency of stiffness, m $(-)$	-	0.41[(3)]	-
Secant stiffness in standard drained triaxial test, E_{50}^{ref} (kN/m^2)	-	55 860[(3)]	-
Tangent stiffness for primary oedometer loading, E_{oed}^{ref} (kN/m^2)	-	55 860[(3)]	-
Unloading-reloading stiffness from drained triaxial tests, E_{ur}^{ref} (kN/m^2)	-	167 580[(3)]	-
Reference shear modulus at very small strains, G_0^{ref} (kN/m^2)	-	123 300[(3)]	-
Threshold shear strain at which $G_s = 0.722 \cdot G_0$, $\gamma_{0.7}$ (%)	-	0.01[(3)]	-

[(1)] After Hamre et al. (2010)
[(2)] Isotropic strength is assumed in the clay layers
[(3)] Derived from $D_r = 93.1\%$ through the empirical expressions proposed by (Brinkgreve et al. (2010))

3. Modelling

3.1. Model formulation

3.1.1. Model design

The macro-element for piles presented in this paper follows the multi-surface plasticity framework, which is encompassed within classical elasto-plastic theory. In elasto-plastic models, the constitutive relation between the generalised load $\boldsymbol{t}$ and the generalised displacement increment $d\boldsymbol{v}$ is established from the following basic components:

1. A principle of adding the elastic and the plastic contributions:

$$d\boldsymbol{v} = d\boldsymbol{v}^e + d\boldsymbol{v}^p \tag{3}$$

   Where $\boldsymbol{v}^e$ and $\boldsymbol{v}^p$ are the generalised elastic and plastic displacement vectors.
2. A relationship that governs the elastic contribution.
3. Ingredients controlling the plastic contribution:
   (a) Yield criterion
   (b) Flow rule
   (c) Hardening law
   (d) Consistency condition

The macro-element model based on multi-surface plasticity behaves as follows. The application of a load increment leads to an elasto-plastic displacement at the pile head. This behaviour is illustrated in Fig. 8 by the non-linear load-displacement curve defined by the points O-A-B, and it is generated in the multi-surface plasticity model by translating the yield surfaces in the $(M/D, H)$ plane. From O to A, the load increment plotted in the $(M/D, H)$ plane lays within the innermost yield surface, and the displacement is only elastic. From A to B, the load path touches and drags the first surface, and plastic displacements are

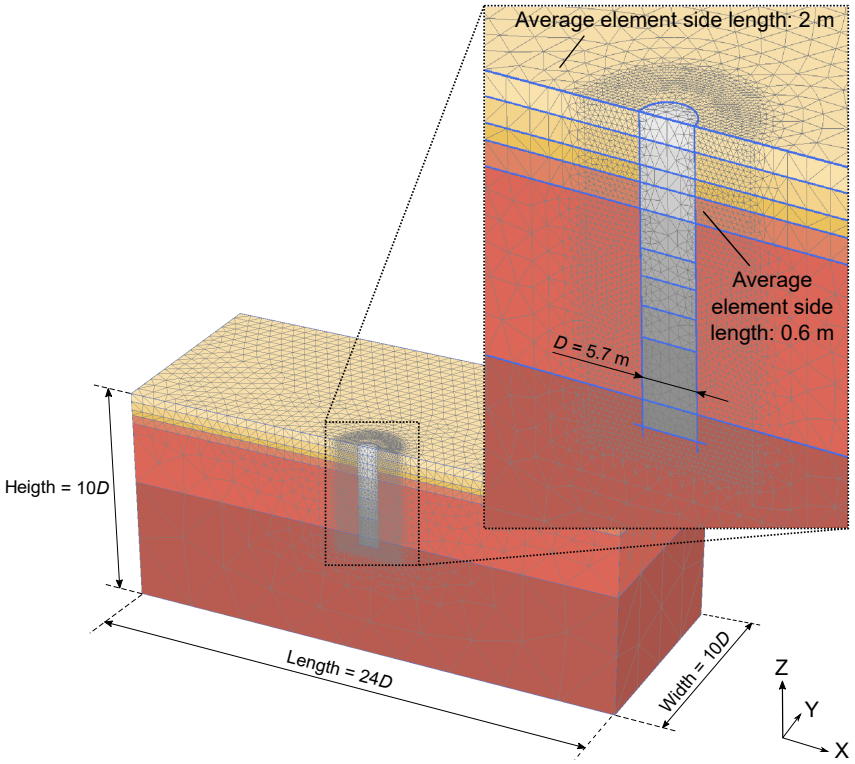

Figure 5: 3D finite element mesh and model dimensions of the Sheringham Shoal reference case. The colour of the soil layers corresponds to the soil units: Bolders Bank (yellow), Egmond Ground (orange) and Swarte Bank (red).

generated. The magnitude of the plastic displacements is function of the resistance of the yield surfaces to translate. The load path eventually touches and drags the second innermost yield surface, and then the plastic displacement generated to the second innermost surface is added to the plastic displacement by the innermost surface. This leads to a piecewise linear load-displacement response. In unloading, as in the path defined by B-C, and in reloading, as in the path defined by C-B-D, the macro-element model behaves in a similar fashion. First, and until the innermost yield surface is reached, the displacement is elastic. Every time a new yield surface is touched, the surface is translated and plastic displacements are generated. In the following sections, the formulation of each of the components of the multi-surface plasticity macro-element model for piles is described. The formulation is based on the trends computed in the FEA of the soil volume and the pile-foundation, and supported by similar expressions from the literature.

3.1.2. Elastic response

The elastic response of the macro-element model is controlled by an elastic stiffness matrix $\boldsymbol{K}$, which relates the generalised force vector $\boldsymbol{t}$ with the generalised elastic displacement $\boldsymbol{v}^e$ as follows:

$$\boldsymbol{t} = \boldsymbol{K} \cdot \boldsymbol{v}^e; \quad \boldsymbol{K} = \begin{bmatrix} k_{11} & k_{12} \\ k_{21} & k_{22} \end{bmatrix} \tag{4}$$

The coefficients of $\boldsymbol{K}$ depend on the pile dimensions, pile properties, soil layering, soil properties and drainage conditions.

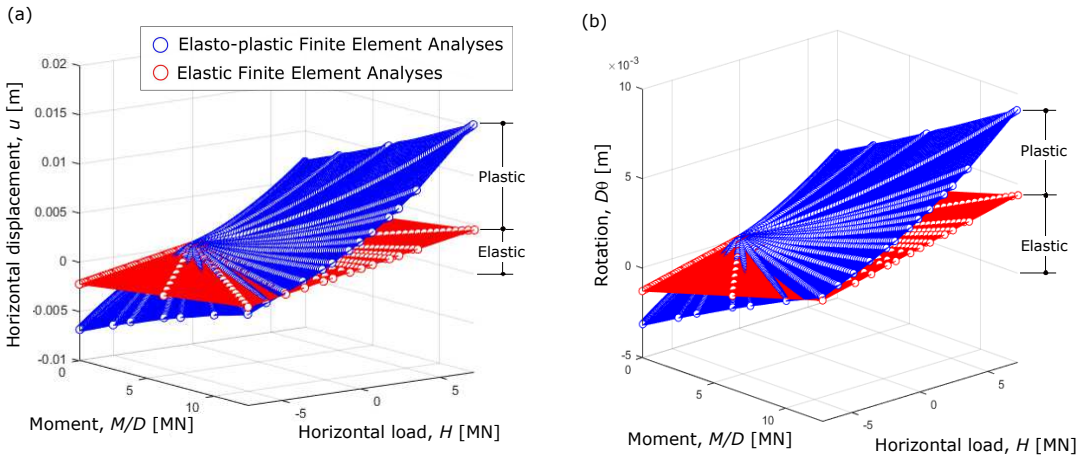

Figure 6: Computed total and elastic response as a function of M/D and H, and linearly interpolated surfaces: (a) horizontal displacement at seabed; (b) rotation at seabed. The difference between the elasto-plastic and the elastic response is the plastic response.

3.1.3. Yield criterion and loading surfaces

The yield criterion f is an equation formulated in terms of generalised forces $\boldsymbol{t}$ and generalised state variables $\boldsymbol{\alpha}$:

$$f(\boldsymbol{t}, \boldsymbol{\alpha}) = f(M/D, H, \alpha_M, \alpha_H) \tag{5}$$

The representation of the yield criterion in the generalised forces space defines yield surfaces. The initial yield criterion defines the limit between the elastic and the elasto-plastic behaviour, while the failure criterion distinguishes between the possible force states from the impossible or non-allowable force states. All the yield surfaces in between these two are known as loading surfaces. The loading surfaces in the macro-element adopt the elliptical shape of the contours of plastic work computed in Section 2.4 and illustrated in Fig. 7a. This assumption follows the work by Mrôz (1967), who described the yield surfaces of a multi-surface plasticity model for materials as contours of constant work-hardening moduli. The yield criterion f_i of surface i is:

$$\begin{aligned} f_i(\boldsymbol{t}, \boldsymbol{\alpha}) = & \\ & \left(\frac{(M/D - \alpha_{M,i}) \cdot \sin\beta + (H - \alpha_{H,i}) \cdot \cos\beta}{b_i} \right)^2 \\ & + \left(\frac{-(M/D - \alpha_{M,i}) \cdot \cos\beta + (H - \alpha_{H,i}) \cdot \sin\beta}{a_i} \right)^2 \\ & - 1 = 0 \end{aligned}$$

Where

- $(\alpha_{M,i}, \alpha_{H,i})$ are the generalised state variables of surface i. They are also found in the literature as the coordinates of the back-stress vector, and they define the position of the centre of the yield surface in the load space.

- a_i and b_i describe the size and β_i describes the orientation of yield surface i , as indicated in Fig. 7a. The orientation β_i and the ratio a_i/b_i are approximately constant for all computed contours of plastic work in Fig. 7a; however, they might vary when the load levels increase and the soil around the pile is further mobilised. The ratio $a/b \approx a_i/b_i$, and the orientation defined by β are assumed

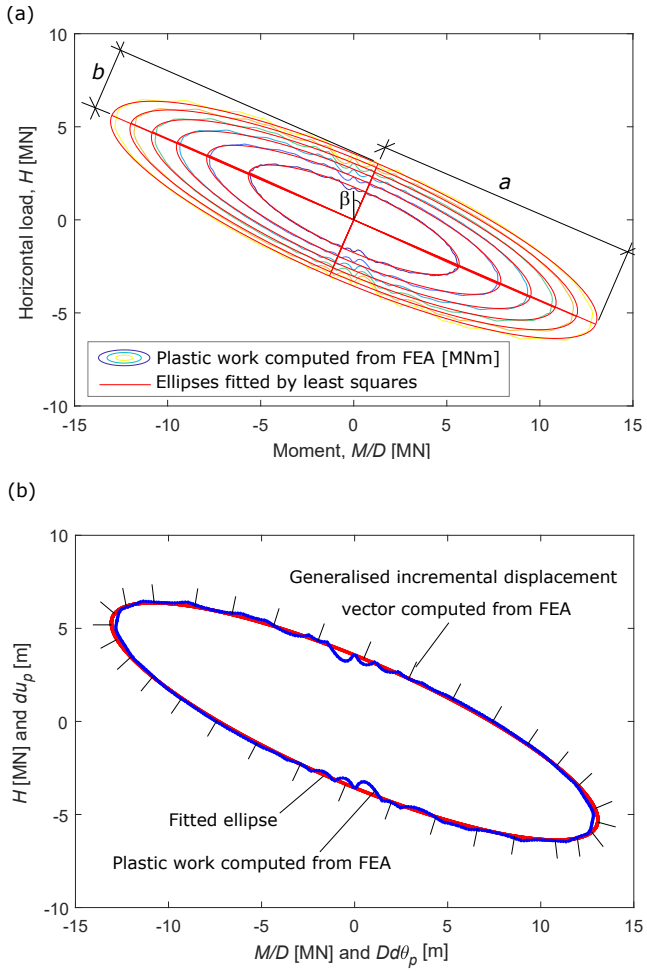

Figure 7: Contours of plastic work W^p computed from Finite Element Analyses (FEA) in the $(M/D, H)$ plane: (a) Ellipses fitted to each contour by least squares; (b) Incremental plastic displacement vectors $(D \cdot d\theta^p, du^p)$.

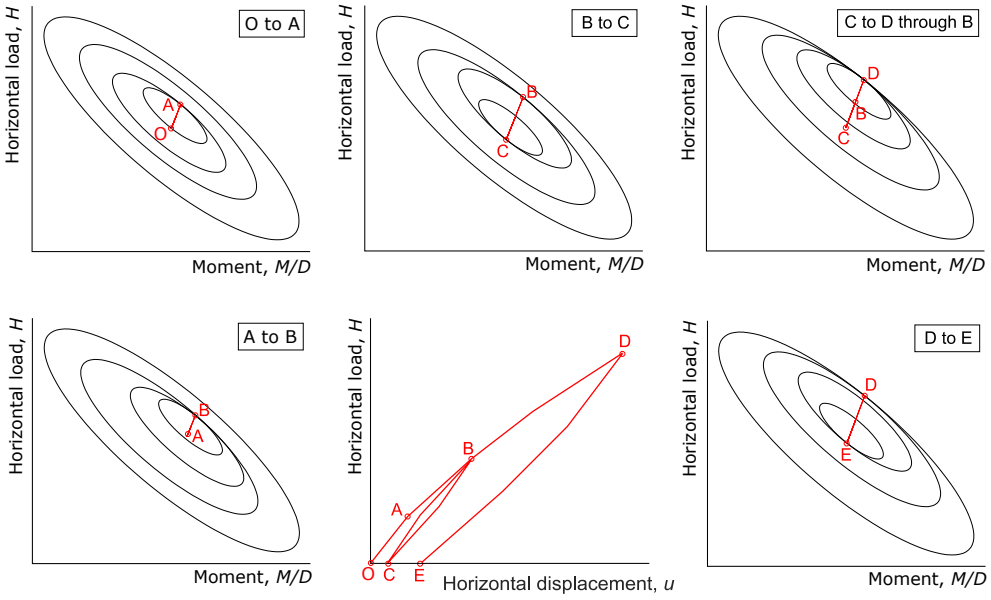

Figure 8: Illustration of the multi-surface plasticity model behaviour based to the translation of the yield surfaces.

to be constant for all the yield surfaces in the macro-element formulation. This implies that the yield surfaces are homothetic to each other.

This yield criterion is comparable to the elliptical yield criterion proposed by Li et al. (2014) for a single elastic pile in sand.

3.1.4. Flow rule

The flow rule defines the direction of the generalised plastic displacement increment $d\boldsymbol{v}^p$, and it can be expressed as the gradient of a plastic potential surface g defined in the load space:

$$d\boldsymbol{v}^p = d\lambda \cdot \frac{\partial g}{\partial \boldsymbol{t}} \tag{6}$$

Where $d\lambda$ is an scalar that determines the magnitude of $d\boldsymbol{v}^p$. When g is equal to the yield surface f, the flow rule is associated. Fig. 7b plots $d\boldsymbol{v}^p$ on top of a yield surface defined by contours of plastic work. The $d\boldsymbol{v}^p$ vectors are normal to the surfaces, which indicates that an associated flow rule can be adopted in the macro-element model formulation. For each yield surface i, $d\boldsymbol{v}_i^p$ is:

$$d\boldsymbol{v}_i^p = d\lambda_i \cdot \frac{\partial f_i}{\partial \boldsymbol{t}} \tag{7}$$

And $d\boldsymbol{v}^p$ is computed as the sum of the plastic contributions of the active yield surfaces assuming Koiter's rule (Koiter, 1953):

$$d\boldsymbol{v}^p = \sum_{i=1}^{j} d\boldsymbol{v}_i^p = \sum_{i=1}^{j} d\lambda_i \cdot \frac{\partial f_i}{\partial \boldsymbol{t}} \tag{8}$$

Where j is the number of active or yielding surfaces, that is, surfaces that are translating in the load space. Note in this formulation, if surface j is active, all the surfaces enclosed by j, that is, from 1 to j, are also active.

3.1.5. Hardening law

The multi-surface plasticity model presented here is of the pure kinematic hardening type, where the yield surfaces do not change in size but only translate in the load space. The kinematic hardening rule defines the direction of $d\boldsymbol{\alpha}$, that is, how do the centre of the yield surfaces translate. In the macro-element model, the kinematic hardening rule proposed by Ziegler (1959), shown in Eq. 9., has been adopted for each yield surface.

$$d\boldsymbol{\alpha}_i = d\mu_i \cdot (\boldsymbol{t} - \boldsymbol{\alpha}_i) \tag{9}$$

Where $d\mu_i$ is function of the scalar $d\lambda_i$, which defines the size of $d\boldsymbol{v}^p$ in the flow rule. Note that for each yield surface i, Ziegler's kinematic hardening rule is only formulated in terms of $\boldsymbol{t}$ and $\boldsymbol{\alpha}_i$, not in terms of other surfaces. This can lead to intersection of the yield surfaces, that is, a violation of the non-intersection condition that some authors prescribe in the formulation of multi-surface plasticity models, see for instance (Mrôz, 1967). The main consequence of having two surfaces intersecting is that instead of having a bi-linear relation between two surfaces, a multilinear relation might be produced (Puzrin and Houlsby, 2001). Puzrin and Houlsby (2001) argue that this is not generally an issue and, in occasions, it can simplify the model implementation. In addition, Montáns and Caminero (2007) demonstrated that in multiaxial predictions using the Mrôz (1967) kinematic hardening rule, where the translation of the surfaces satisfies a non-intersection condition: (1) the multi-surface plasticity model response depended on the number of yield surfaces used in the calibration; and (2) Mrôz's kinematic hardening rule lead to uncontrolled multiaxial ratcheting, while the uniaxial response did not show ratcheting. In that sense,

Ziegler's kinematic hardening rule does not depend on the number of surfaces and does not predict multiaxial ratcheting, which is more consistent with the uniaxial behaviour. This translation rule can also be expressed as in Grimstad et al. (2014) by multiplying $d\boldsymbol{v}^p$ by the plastic stiffness matrix $\boldsymbol{K}_i^p$, as indicated in Eq. 10.

$$d\boldsymbol{\alpha}_i = \boldsymbol{K}_i^p \cdot d\boldsymbol{v}^p = d\lambda_i \cdot \boldsymbol{K}_i^p \cdot \frac{\partial f_i}{\partial \boldsymbol{t}} \tag{10}$$

Note that the plastic stiffness matrix $\boldsymbol{K}_i^p$ is interpreted as a ratio between $(\boldsymbol{t} - \boldsymbol{\alpha}_i)$ and $d\boldsymbol{v}^p$. For each yield surface i, the plastic stiffness matrix $\boldsymbol{K}_i^p$, is constant, which leads to piece-wise linear hardening curves.

3.1.6. Consistency condition

In addition to the yield criterion, the flow rule and the kinematic hardening rule, the consistency condition is needed to find $d\lambda_i$ of each yield surface. In a kinematic hardening model with a single yield surface, the consistency condition can be expressed as indicated in Eq. 11.

$$df = \left(\frac{\partial f}{\partial \boldsymbol{t}}\right)^T \cdot d\boldsymbol{t} + \frac{\partial f}{\partial \boldsymbol{\alpha}} \cdot \frac{\partial \boldsymbol{\alpha}}{\partial \lambda} \cdot d\lambda = 0 \tag{11}$$

Often $\frac{\partial f}{\partial \boldsymbol{\alpha}} \cdot \frac{\partial \boldsymbol{\alpha}}{\partial \lambda}$ is expressed as $-A$, the plastic resistance, and Eq. 11 can be rewritten as follows:

$$A \cdot d\lambda = \left(\frac{\partial f}{\partial \boldsymbol{t}}\right)^T \cdot d\boldsymbol{t} \approx f; \quad f \approx A \cdot d\lambda \tag{12}$$

If instead of having one active yield surface, the model has j active yield surfaces, the consistency condition can be expressed as:

$$\boldsymbol{f} = \begin{bmatrix} f_1 \\ f_2 \\ \vdots \\ f_j \end{bmatrix} \approx \begin{bmatrix} a_{11} + A_1 & a_{12} & \dots & a_{1j} \\ a_{21} & a_{22} + A_2 & \dots & a_{2j} \\ \vdots & \vdots & \ddots & \vdots \\ a_{j1} & a_{j2} & \dots & a_{jj} + A_j \end{bmatrix} \cdot \begin{bmatrix} d\lambda_1 \\ d\lambda_2 \\ \vdots \\ d\lambda_j \end{bmatrix} = \boldsymbol{\Xi} \cdot d\boldsymbol{\lambda} \tag{13}$$

Where

$$a_{ik} = \left(\frac{\partial f_i}{\partial \boldsymbol{t}}\right)^T \cdot \boldsymbol{K} \cdot \left(\frac{\partial g_k}{\partial \boldsymbol{t}}\right) \tag{14}$$

And

$$A_k = \left(\frac{\partial f_k}{\partial \boldsymbol{t}}\right)^T \cdot \boldsymbol{K}_k^p \cdot \left(\frac{\partial g_k}{\partial \boldsymbol{t}}\right) \tag{15}$$

The derivation of Eq. 13 and the coefficients a_{ik} and A_k (Eqs. 14 and 15) are documented in detail in Skau et al. (2017).

3.2. Numerical Implementation

The macro-element model has been implemented in the OWT simulation software *3DFloat* (Nygaard et al., 2016) via a *dll* (Dynamic Link Library) interface. In each iteration of a calculation step, *3DFloat* passes on displacements and rotations ($\Delta\boldsymbol{v}$) at seabed to the foundation model, which transfers back the computed forces and moments $\boldsymbol{t}$. The numerical implementation of the macro-element model solves the incremental relation:

$$\boldsymbol{t} = \boldsymbol{t}_0 + \Delta\boldsymbol{t} = \boldsymbol{t}_0 + \boldsymbol{K} \cdot \Delta\boldsymbol{v}^e = \boldsymbol{t}_0 + \boldsymbol{K} \cdot (\Delta\boldsymbol{v} - \Delta\boldsymbol{v}^p) \tag{16}$$

Where $\boldsymbol{t}_0$ is the generalised force at the begining of the step. The incremental relation from Eq. 16 is solved following an explicit integration algorithm, where $f_i = 0$ is enforced at the end of the step. If the condition $f_i \approx 0$ is not satisfied after a certain number of iterations, an automatic substepping algorithm is called.

A change in the coordinate system has been applied to simplify the macro-element model implementation and make it more robust. In this change, the axes $(M/D, H)$ in the load plane are rotated and squeezed such as the elliptical yield surfaces are displayed as circles. Consequently, the yield criterion can be formulated as a circle with a radius defined by a load invariant, which is function of the two load components. This is done by employing a linear transformation matrix $\boldsymbol{R}$:

$$\boldsymbol{t}' = \boldsymbol{R} \cdot \boldsymbol{t} = \begin{bmatrix} \cos\beta & a/b \cdot \sin\beta \\ \sin\beta & a/b \cdot \cos\beta \end{bmatrix} \cdot \boldsymbol{t} \tag{17}$$

Where $\boldsymbol{t}'$ is the generalised load vector in the transformed axes system, a/b describes the shape of the elliptical yield surfaces and β describes its orientation, as illustrated in Fig. 7a. Note that this change can only be applied when all the yield surfaces are homothetic to each other. The incremental displacement $\Delta\boldsymbol{v}$ is transformed accordingly with the inverse of the transpose of $\boldsymbol{R}$, i.e. the $(\boldsymbol{R}^T)^{-1}$ matrix.

$$\Delta\boldsymbol{v}' = (\boldsymbol{R}^T)^{-1} \cdot \Delta\boldsymbol{v} \tag{18}$$

Where $\Delta\boldsymbol{v}'$ is the generalised displacement increment in the transformed axes system. It can be proven that the plastic work does not vary with the reference system, that is, whether it is calculated in the initial system of coordinates or in the transformed system of coordinates:

$$\begin{aligned} \Delta W^p = & \\ & (\boldsymbol{t}')^T \cdot \Delta\boldsymbol{v}'_p = (\boldsymbol{R} \cdot \boldsymbol{t})^T \cdot ((\boldsymbol{R}^T)^{-1} \cdot \Delta\boldsymbol{v}_p) = \\ & = \boldsymbol{t}^T \cdot \boldsymbol{R}^T \cdot (\boldsymbol{R}^T)^{-1} \cdot \Delta\boldsymbol{v}_p = \boldsymbol{t}^T \cdot \Delta\boldsymbol{v}_p \end{aligned} \tag{19}$$

Before the constitutive equation is solved, $\Delta\boldsymbol{v}$ and the loads from the previous load step $\boldsymbol{t}_0$ are transferred into the transformed coordinate system by employing $\boldsymbol{R}$ and $(\boldsymbol{R}^T)^{-1}$. Then the constitutive relation is solved in the transformed axes system and the calculated generalized forces are transformed back to the original coordinate system.

3.3. Model calibration

The calibration of the foundation model requires two types of input: (1) the coefficients of the elastic stiffness matrix and (2) load-displacement curves from non-linear analyses. The elastic stiffness matrix is used to predict the elastic response, and the non-linear load-displacement curves are employed to derive the shape and size of the yield surfaces and the hardening law. This last derivation is performed internally by the macro-element model.

For homogeneous soil profiles, the elastic stiffness matrix coefficients can be obtained from semi-empirical formulae, see for instance Randolph (1981), Gazetas (1991) or Shadlou and Bhattacharya (2016). For layered soil profiles, or for changes in soil stiffness with depth not considered in these semi-empirical formulae, theses coefficients can be obtained from Shadlou and Bhattacharya (2014), from FEA by modelling the pile and the soil as linear elastic materials, or from boundary element analyses, see for instance Kaynia and Kausel (1982).

The non-linear load-displacement curves can be obtained from static pushover FEA with a soil model that represents the relevant cyclic nonlinear response. Reference is made to (Andersen, 2015, Kaynia and

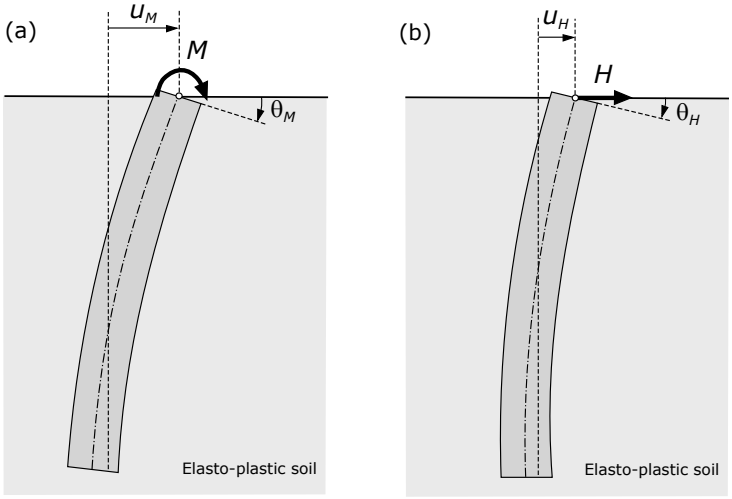

Figure 9: Loading conditions adopted in the analyses to determine the non-linear load-displacement curves at seabed for the macro-element calibration: (a) an overturning moment; (b) a horizontal load.

Andersen, 2015, Skau and Jostad, 2014) for more information regarding the use of FEA to compute cyclic foundation response based on soil element behaviour. Alternatively, model test data can be employed. Two analyses or tests (see Fig. 9) are required to establish these curves: (1) a pushover analyses where a moment is applied at the pile head at seabed, from which $M - u_M$ and $M - \theta_M$ curves are obtained, and (2) a pushover analyses where a horizontal load is applied at the pile head at seabed, from which $H - u_H$ and $H - \theta_H$ curves are obtained. Altogether four curves are given as input in a tabulated form.

The macro-element model is calibrated internally as follows. First, it computes the plastic displacements as the difference between the elasto-plastic and the elastic components. Then, it determines the coefficients a/b and β from the relations between the loads and the plastic displacements. After, it builds the transformation matrix $\boldsymbol{R}$ following Eq. 17. The load-plastic displacement relations are transferred to the transformed axis system, where the yield surfaces are circular and the same response is obtained in any radial direction. From the transformed load-plastic displacement relations, the radius S_i, and the plastic stiffness matrix $\boldsymbol{K}_i^p = K_i^p \cdot \boldsymbol{I}$ associated to each yield surface are calculated following the assumption that the yield surfaces are coupled in series. An sketch of the series coupled system can be found for instance in Grimstad et al. (2014).

4. Performance of the macro-element model

4.1. Test examples

The performance of the macro-element model is illustrated and compared against numerical simulations and field tests for the three examples described in Table 2. In each example, the selected site conditions, pile dimensions and loading paths are representative for piles supporting monopile-based OWTs.

4.2. Example A: Verification against monotonic finite element analyses

The aim of this example is to illustrate the performance of the macro-element model and verify the response against the FEA used as a basis for the model formulation. The soil conditions, pile dimensions and numerical model employed in Example A are described in detail in Section 2.3. The macro-element model is calibrated from load-displacement curves computed by FEA. In the comparison, displacement-controlled radial paths, where the ratio between u and $D \cdot \theta$ at the pile head is kept constant, are applied

Table 2: Overview of the examples used to show the macro-element performance and its comparison against numerical analyses and field tests.

Name	Example A	Example B	Example C
Comparison against	Monotonic Finite Element Analyses	Cyclic Finite Element Analyses	Field tests
Site description	Layered soil profile at the Sheringham Shoal offshore wind farm, United Kingdom	Idealised clay profile	Clay profile at Cowden, United Kingdom
Soil layering	Bolders Bank Formation: firm to stiff clay; Egmond Ground Formation: dense to very dense sand; Swarte Bank Formation: stiff to hard sandy-gravelly clay	Homogeneous clay with varying undrained shear strength and stiffness with depth	Glacial, ductile, low plasticity stiff clay with varying undrained shear strength and stiffness with depth
Main soil properties			
Unit Weight, γ (kN/m^3)	19.0-21.3	18.0	21.2
Average shear modulus at very small strains, G_{max} (MN/m^2)	200	75	100
Average undrained shear strength, s_u (kPa)	150	200	120
Shear strain at failure, γ_f (%)	16-20	15	30
Pile dimensions			
Diameter, D (m)	5.7	6.0	0.762
Length, L (m)	28.5	24.0	4.00 - 7.62
Wall thickness, t (m)	0.060	0.060	0.011 - 0.025
L/D $(-)$	5	4	5-10
D/t $(-)$	95	100	69-30

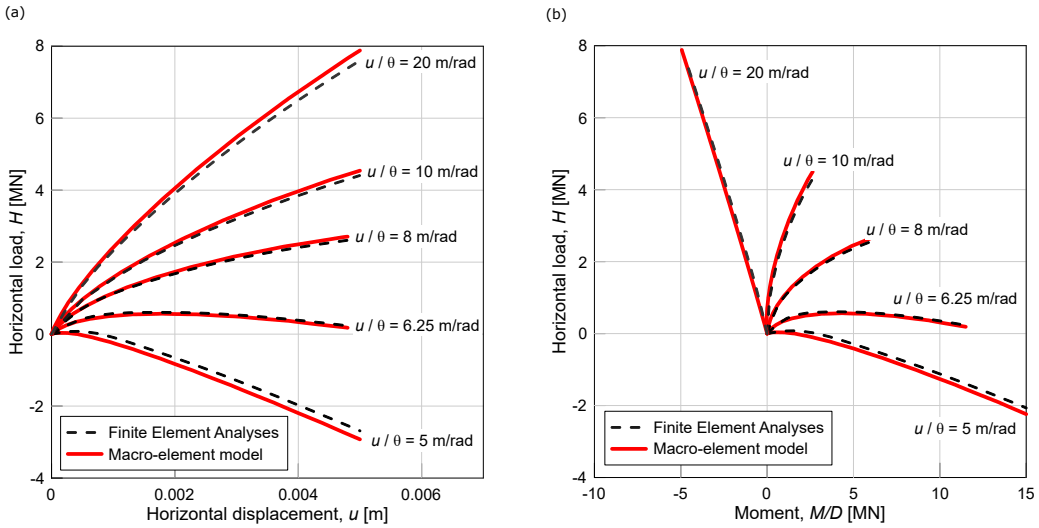

Figure 10: Example A: Comparison between the macro-element model and monotonic FEA in displacement-controlled radial tests with constant u/θ ratios.

at the pile head. The computed moments are in the range of the measured moments at seabed for one of the monopiles at Sheringham Shoal during idling conditions, where the OWT is subjected to average wind speeds in the order of 25 to 27 m/s and significant wave heights of 2.6 to 2.8 m. The comparison between the macro-element model and the monotonic FEA is presented in Fig. 10. Good agreement is found for all the paths evaluated. In particular, the macro-element captures well the load-displacement curves, and it is also capable of reproducing correctly the coupling between M/D and H seen in the FEA.

4.3. Example B: Verification against cyclic finite element analyses

The objective of Example B is to illustrate the performance of the macro-element during cyclic loading and verify the response against cyclic FEA. The applied loads roughly correspond to maximum ULS loads from an OWT installed in the North Sea. The cyclic loads are applied in the simulations statically, which means that the frequency dependency of stiffness and damping is not included in the FEA. Thus, the only damping contribution comes from the material or hysteretic damping of the constitutive soil model. The frequency dependency of the foundation response has not been included in the FEA because, for typical soil conditions found in OWTs, it can be neglected at low frequencies.

The pile modelled in Example B is a steel pile with a diameter of 6 m, a wall thickness of 0.06 m, and an embedded length of 24 m. The pile dimensions lead to a length-to-diameter ratio of 4, which may be expected in the next generation of monopiles supporting offshore wind turbines. The soil consists of a homogeneous isotropic clay layer with strength and stiffness according to the profile illustrated in Fig. 11.

A constitutive model for cohesive materials that is capable of reproducing unloading and reloading, similar to the model proposed by Grimstad et al. (2014), has been employed. The model is a multi-surface plasticity model with kinematic hardening, where the yield surfaces are defined by the Von Mises criterion, the flow rule is associative, and the kinematic hardening is based on Prager's translation rule (Prager, 1955). The model follows Masing's rule (Masing, 1926), and does not account for accumulation of strains in the soil due to cyclic loading. The constitutive model behaviour is illustrated in Fig. 12 for the clay in Example B. The FE-model used to calibrate the macro-element model and to perform the simulations of cyclic tests in Example B follows the modelling assumptions described in Section 2.3.

Fig. 13 displays the comparison between the macro-element model and the cyclic FEA. The applied loading at the pile head includes changes in the load direction $\Delta M/\Delta H$ and load eccentricity M/H.

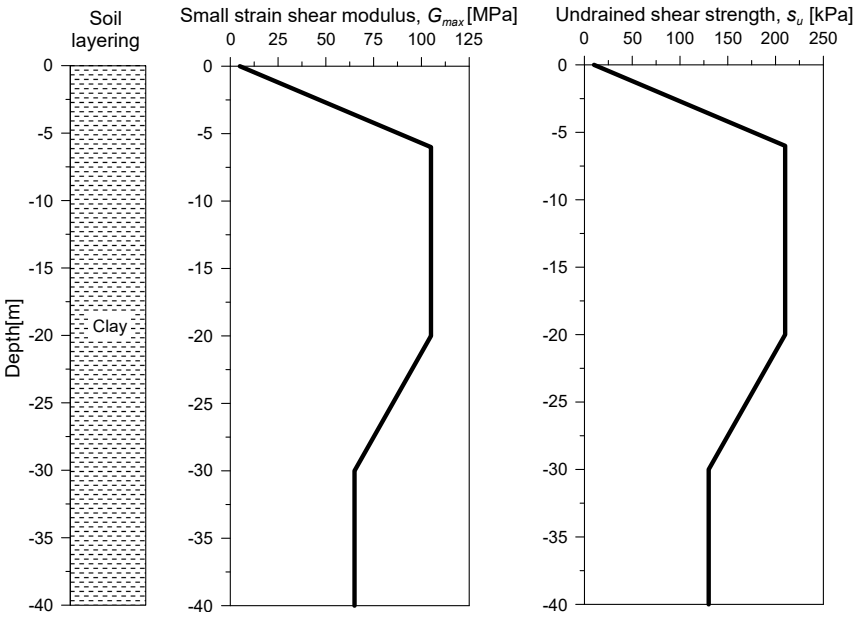

Figure 11: Example B: Idealised clay profile employed in the comparison.

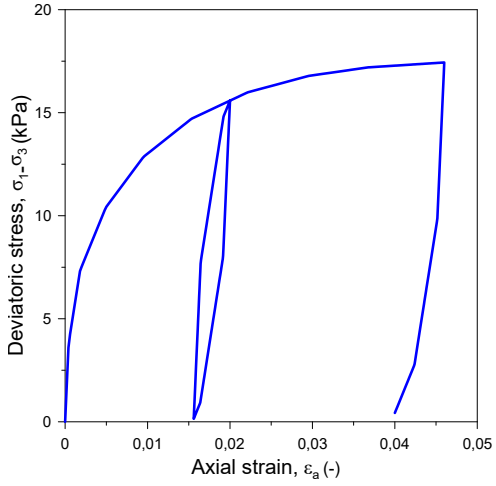

Figure 12: Example B: Simulated deviatoric stress axial strain response from an undrained triaxial test employing the constitutive model for clays.

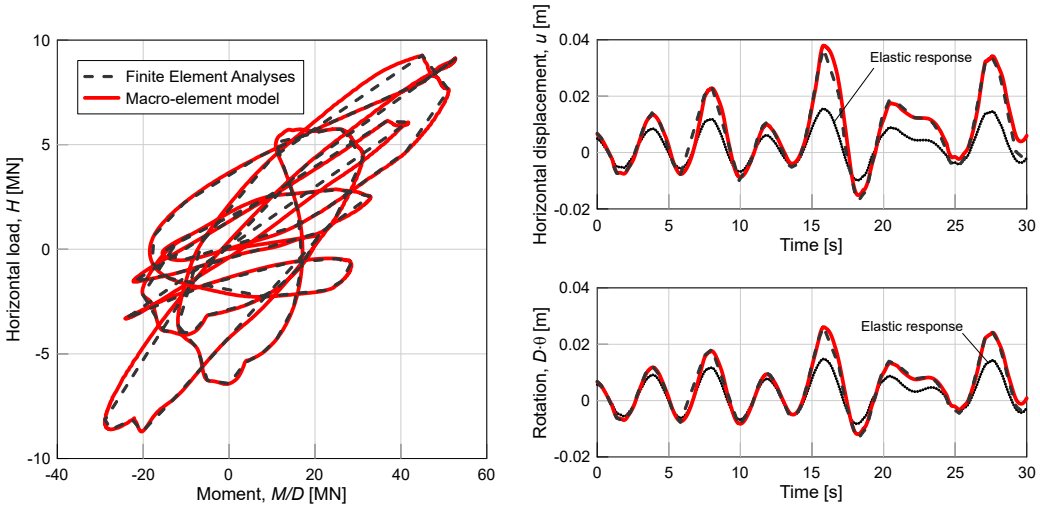

Figure 13: Example B: Comparison between the macro-element model and cyclic finite element analyses for an irregular load-controlled time history.

The load eccentricity M/H is extracted from the integrated load simulations of a monopile-based OWT subjected to a turbulent wind speed of 26 m/s presented in Aasen et al. (2017). The applied maximum loads roughly correspond to the ULS loads from an OWT installed in the North Sea.

The horizontal displacements and rotations predicted by the macro-element model match the results from cyclic FEA very well. This indicates that the macro-element model can reproduce accurately varying load conditions, which are expected in time-domain integrated load simulations. Fig. 13 also displays the elastic component of the horizontal displacements and rotations. It is worth noting that even at load levels corresponding to ULS, more than half of the computed horizontal displacements and rotations are elastic.

4.4. Example C: Comparison with field tests

The aim of this example is to demonstrate that the macro-element model calibrated by FEA can reproduce the experimental response from the lateral pile field tests documented in Byrne et al. (2017). The test site is located at Cowden (on the north east coast of England), and consists on glacial, ductile, low plasticity stiff clay (Byrne et al., 2017). Fig. 14 illustrates the compression undrained shear strength and maximum shear modulus of the soil with depth derived from field and laboratory tests (Powell and Butcher, 2003, Zdravković et al., 2015, Byrne et al., 2017), together with the profile selected in the calibration by FEA.

The FE-model employed in the calibration of the macro-element model is based on the following assumptions: only half of the geometry and the loads are included; interface elements are applied between the pile and the soil; fixed boundary conditions are applied at the base and roller boundaries are applied at the lateral boundaries; and the pile is modelled with solid elements with linear elastic properties. The stiffness and compression strength of the interface is equivalent to that of the soil, while the interface tension strength is governed by a no-tension criterion that allows gap opening between the soil and the pile. The soil behaviour is modelled undrained using the NGI-ADP constitutive model (Grimstad et al., 2012). The constitutive model calibration, displayed in Fig. 15, is based on isotropically consolidated triaxial undrained compression tests and modulus reduction laboratory data (Powell and Butcher, 2003). Note that the NGI-ADP constitutive model overestimates the stiffness in Fig. 15 (right) while it underestimates the stiffness in Fig. 15 (left). In addition, Zdravković et al. (2015) state that the in-situ geophysics revealed anisotropy typical of overconsolidated clays; however there is a lack of data quantifying it. In

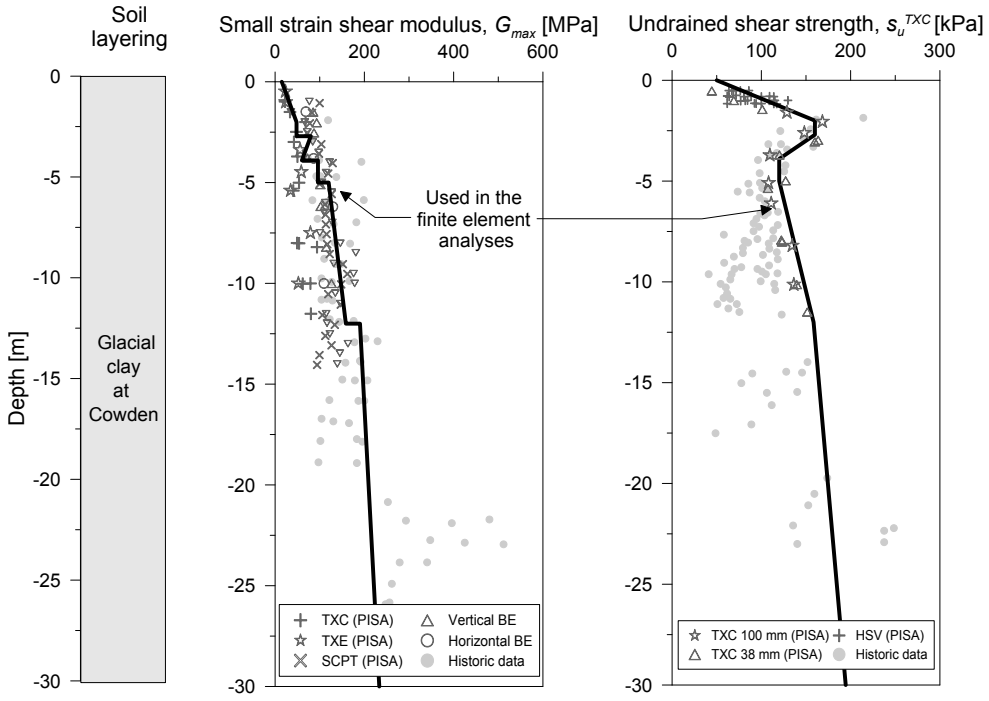

Figure 14: Example C: Field and laboratory tests from the Cowden test site after Powell and Butcher (2003), Zdravković et al. (2015), Byrne et al. (2017). TXC (triaxial compression test), HSV (hand shear vane), TXE (triaxial extension test), BE (bender element test), SCPT (seismic cone penetrometer test). The soil line plots the profiles used in the calibration by FEA.

order to account for the variation in stiffness and strength in the different directions, it is assumed that the strength ratios of the clay at Cowden are comparable to the strength ratios of Drammen clay, which is a clay with a similar plasticity index ($PI \approx 20\%$) and a similar overconsolidation ratio ($OCR \approx 40$). Based on the strength ratios from Drammen clay documented in Andersen et al. (1980), a strength ratio of $s_u^{DSS}/s_u^{TXC} = 0.71$ in Direct Simple Shear and a strength ratio of $s_u^{TXE}/s_u^{TXC} = 0.55$ in triaxial extension are assumed in the FEA used to calibrate the model.

In Example C, two tests are compared to the macro-element results: one with an embedded length of $L = 7.62$ m and another with $L = 4$ m. Both tests are performed on tubular steel piles with a diameter of $D = 0.762$ m and a nominal steel thickness of 25 mm and 11 mm (Byrne et al., 2015), respectively. This leads to length-to-diameter ratios of $L/D = 10$ and $L/D = 5.25$, which can be representative for piles supporting OWTs.

Figs. 16 and 17 illustrate the comparison between the field test results and the macro-element model prediction. It is apparent that the macro-element model can reproduce the measured load-displacement response of the field tests. In particular, the pile-soil stiffness during loading and unloading is correctly captured at low load amplitudes. During unloading, the response computed by the macro-element model is to a small extent stiffer than the measured response.

5. Limitations of the macro-element model

There are limitations in the application of the macro-element model presented in this paper, mostly due to the assumptions adopted in the model formulation:

- The coupling between horizontal load and moment is only included in planar load conditions. This

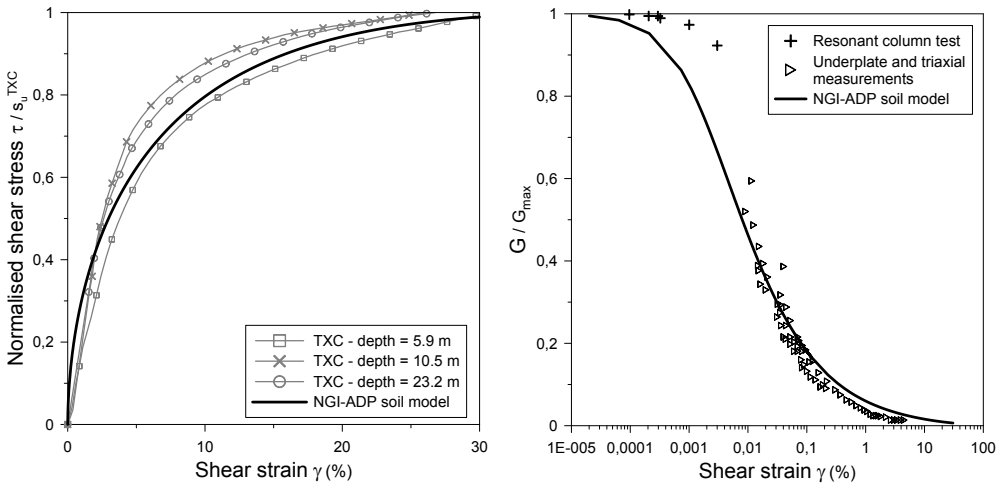

Figure 15: Example C: Comparison between the calibrated NGI-ADP soil model and the laboratory tests documented in Powell and Butcher (2003)

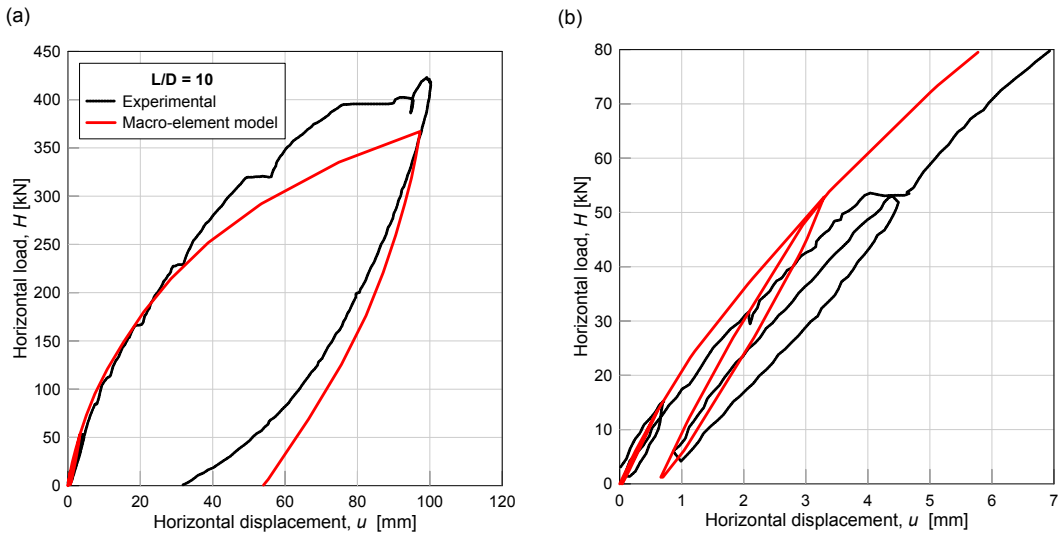

Figure 16: Example C: Comparison between the macro-element model and experimental results from field tests with $L/D = 10$: (a) Overall response; (b) Small displacement response.

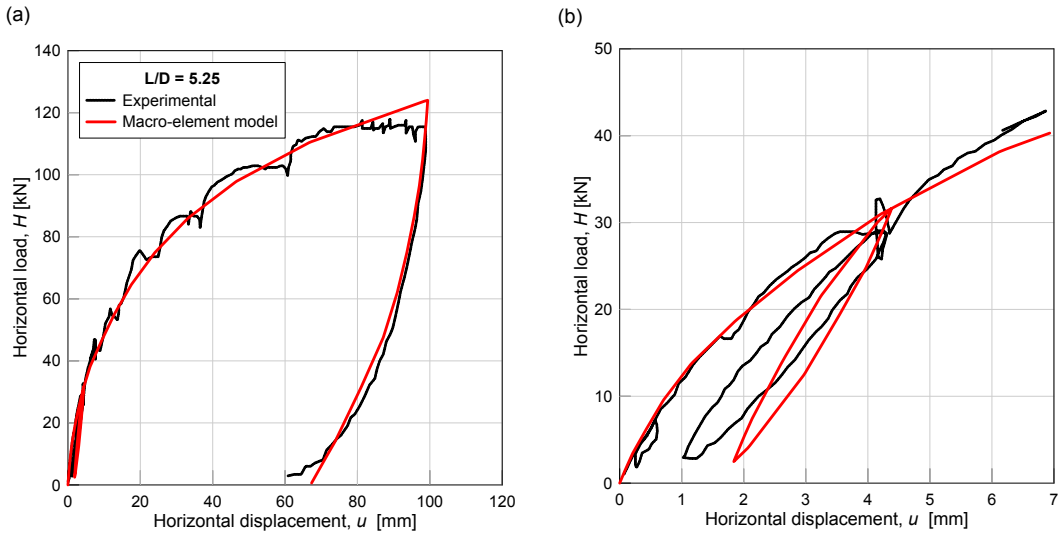

Figure 17: Example C: Comparison between the macro-element model and experimental results from field tests with $L/D = 5.25$: (a) Overall response; (b) Small displacement response.

means that interaction between e.g. two horizontal loads perpendicular to each other is not taken into account in the macro-element model.

- The effect of the vertical load on the lateral response is not explicitly accounted for in the model formulation. For piles supporting monopile-based OWTs and for the load levels considered, different parts of the soil volume are mobilised when a vertical load and a lateral load are applied. Therefore, the interaction between the vertical load and the horizontal and moment loads is not expected to be significant and it has not been included in the model formulation. If considered necessary, the effect of the vertical load on the lateral load response can be included indirectly by calibrating the macro-element at the relevant vertical load level.

- The macro-element model is formulated and verified employing results from FEA, which include some assumptions. The main assumptions considered in the FEA are: (1) the response of the pile and the soil is independent of frequency; and (2) the soil conditions considered are homogeneous clay profiles or layered soil profiles where clay is predominant. These assumptions limit the applicability of the macro-element model to similar conditions or to cases where these assumptions are acceptable.

- The macro-element model is rate-independent, that is, it provides foundation stiffness and damping independently of the applied loading frequency and does not include the inertia of the soil. The frequency dependency has not been included in the model formulation because, for typical soil conditions found in offshore wind farms, it can be neglected at low frequencies. For the pile and soil conditions presented in Section 2, the threshold frequency calculated with the formulae from Shadlou and Bhattacharya (2014) is approximately 1.3 Hz. The first natural frequency of monopile-based OWTs typically lies between 0.25 and 0.35 Hz (Shadlou and Bhattacharya, 2016). This implies that the first natural frequency is way below the threshold, and therefore no noticeable frequency dependence is expected.

- The yield surfaces are assumed to be homothetic to each other in the macro-element model formulation. For the load ranges presented in this paper, this assumption seems to be acceptable. However, results from FEA at higher load levels indicate that the yield surfaces may change their

orientation and shape when the soil is further mobilised (Skau et al., 2017). If this is the case, a reduction in the macro-element model accuracy may be expected.

- The kinematic hardening rule assumed in the macro-element formulation follows Masing's rule. This is a reasonable assumption when the pile is subjected to relatively low load levels and the opening of a gap between the pile and the soil is not expected. However, if a gap is generated, a stiffer and more non-linear macro-element response can be expected, which results in unrealistic hysteretic damping. This can be solved by calibrating the macro-element model to a cyclic load-displacement curve as proposed by Kaynia and Andersen (2015), where the effect of cyclic loading, in this case the effect of gap opening, is taken into account.

6. Conclusions

In this paper, a macro-element model for piles in cohesive soils is presented with the objective of providing a simple, efficient and accurate tool for modelling the foundation response in integrated time-domain simulations of monopile-based OWTs. The macro-element model reproduces the response of a pile and the surrounding soil by relating the generalised force and displacement at seabed. The macro-element model is formulated in the multi-surface plasticity framework, and it represents a new application of this framework.

The macro-element model formulation is based on results from FEA of the soil and the foundation, where the pile geometry and soil conditions are selected from a real offshore wind farm. Focus is set on reproducing the load-displacement response of a pile supporting a monopile-based OWT, where an accurate prediction of stiffness and damping is crucial to perform reliable fatigue analyses. The macro-element formulation is comparable to those of similar macro-element models. However, the presented model differs from other macro-element models for piles in the treatment of accumulated displacements. The macro-element model does not accumulate displacements as a function of the number of cycles, neither in a controlled nor in an uncontrolled manner. This is consistent with the premise that significant accumulated displacements are not expected for the relatively low load levels (compared to the pile capacity) and for the number of cycles present in the 10 to 60 minutes long time windows considered in integrated load simulations.

The macro-element model input is simple and intuitive, where non-linear load-displacement curves representing the pile and soil response to monotonic lateral loading are required. Despite these curves can be calculated using different methods, it is suggested to employ 3D FEA in combination with constitutive models that can accurately reproduce the soil behaviour. Alternatively, experimental results from model tests can be used to calibrate the model. Note that the accuracy of the macro-element is directly linked to the accuracy of the load-displacement curves employed in the calibration. In order to obtain accurate predictions with the macro-element model, the results from FEA or model tests used in the calibration should reproduce the pile behaviour accurately.

The performance of the macro-element model has been compared against field test measurements and against results from finite element analyses for three piled foundations. The comparison between the macro-element prediction and field tests indicates that the macro-element model can reproduce the non-linear load-displacement response and the hysteretic behaviour observed in piled foundations with different L/D ratios. In addition, very good agreement is found between the macro-element predictions and the FEA results. This confirms that, for the load levels considered, the macro-element model can reproduce the pile and surrounding soil system behaviour with the same level of accuracy as the FEA, but with a considerable reduction of the computational cost. This is important for practical applications,

where the response of the foundation in time-domain analyses has to be computed for thousands of load cases.

The macro-element model was developed primarily for modelling the soil and pile response in integrated time-domain simulations of monopile-based offshore wind turbines. On this regard, the macro-element model is implemented in an OWT load simulation code, *3DFloat*, via a *dll* interface. However, the macro-element model is not necessarily limited to this application, and it may be used to predict the pile foundation response in applications where response of the piled foundation to lateral loading in the time-domain analyses is relevant, such as offshore structures or bridges.

7. Acknowledgements

The financial support by the Norwegian Research Council through the project *Reducing cost of offshore wind by integrated structural and geotechnical design (REDWIN)*, Grant No. 243984, is gratefully acknowledged. The constructive comments and suggestions given by Kristoffer Skjolden Skau and Amir M. Kaynia are also appreciated.

8. References

Aasen, S., Page, A. M., Skau, K. S. and Nygaard, T. A. (2017), 'Effect of foundation modelling on the fatigue lifetime of a monopile-based offshore wind turbine', *Wind Energy Science* **2**(2), 361.

American Petroleum Institute (2014), *Recommended Practice 2A-WSD. Planning, Designing, and Constructing Fixed Offshore Platforms - Working Stress Design*, 22 edn, American Petroleum Institute.

Andersen, K. H. (2015), Cyclic soil parameters for offshore foundation design, *in* 'Frontiers in Offshore Geotechnics III', CRC Press.

Andersen, K. H., Rosenbrand, W. F., Brown, S. F. and Pool, J. H. (1980), 'Cyclic and static laboratory tests on drammen clay', *Journal of the Geotechnical Engineering Division* **106**(5), 499–529.

Arany, L., Bhattacharya, S., Macdonald, J. and Hogan, S. (2017), 'Design of monopiles for offshore wind turbines in 10 steps', *Soil Dynamics and Earthquake Engineering* **92**, 126–152.

Arshad, M. and O'Kelly, B. C. (2016), 'Analysis and design of monopile foundations for offshore wind-turbine structures', *Marine Georesources & Geotechnology* **34**(6), 503–525.

Benz, T. (2007), Small-strain stiffness of soils and its numerical consequences, PhD thesis, Institut für Geotechnik, Universität Stuttgart, Pfaffenwaldring 35, 70569 Stuttgart.

Beuckelaers, W. (2015), 'Fatigue life calculation of monopiles for offshore wind turbines using a kinematic hardening soil model', *Ground Engineering* pp. 26–29.

Beuckelaers, W., Burd, H. and Houlsby, G. (2017), Integrated design method of monopile foundations for offshore wind turbines using a kinematic hardening soil model, *in* 'Proceedings of OSIG 2017 Conference', Society for Underwater Technology.

Bienen, B., Byrne, B., Houlsby, G. and Cassidy, M. (2006), 'Investigating six-degree-of-freedom loading of shallow foundations on sand', *Géotechnique* **56**(6), 367–379.

Brinkgreve, R., Engin, E. and Engin, H. (2010), Validation of empirical formulas to derive model parameters for sands, *in* 'Numerical methods in geotechnical engineering', CRC Press/Balkema, Rotterdam, the Netherlands, pp. 137–142.

Brinkgreve, R., Kumarswamy, S. and Swolfs, W. (2015), *PLAXIS 2015. Reference Manual*, Plaxis bv.

Butterfield, R., Houlsby, G. T. and Gottardi, G. (1997), 'Standardized sign conventions and notation for generally loaded foundations', *Géotechnique* **47**(5), 1051–4.

Byrne, B., McAdam, R., Burd, H., Houlsby, G., Martin, C., Beuckelaer, W., Zdravkovic, L., Taborda, D., Potts, D., Jardine, R. et al. (2017), PISA: new design methods for offshore wind turbine monopiles, *in* 'Proceedings of the Society for Underwater Technology Offshore Site Investigation and Geotechnics 8th International Conference on Smarter Solutions for Future Offshore Developments'.

Byrne, B., McAdam, R., Burd, H., Houlsby, G., Martin, C., Zdravković, L., Taborda, D., Potts, D., Jardine, R., Sideri, M. et al. (2015), New design methods for large diameter piles under lateral loading for offshore wind applications, *in* '3rd International Symposium on Frontiers in Offshore Geotechnics (ISFOG 2015), Oslo, Norway, June', pp. 10–12.

Correia, A. (2011), A pile-head macro-element approach to seismic design of monoshaft-supported bridges, PhD thesis, European School for Advanced Studies in Reduction of Seismic Risk (ROSE School), Pavia, Italy.

Cremer, C., Pecker, A. and Davenne, L. (2001), 'Cyclic macro-element for soil–structure interaction: material and geometrical non-linearities', *International Journal for Numerical and Analytical Methods in Geomechanics* **25**(13), 1257–1284.

Damgaard, M., Ibsen, L. B., Andersen, L. V. and Andersen, J. (2013), 'Cross-wind modal properties of offshore wind turbines identified by full scale testing', *Journal of Wind Engineering and Industrial Aerodynamics* **116**, 94–108.

Damgaard, M., Zania, V., Andersen, L. V. and Ibsen, L. B. (2014), 'Effects of soilstructure interaction on real time dynamic response of offshore wind turbines on monopiles', *Engineering Structures* **75**, 388–401.

De Vries, W., Versteijlen, W., Metrikine, A., Hoving, J. and Smidt, E. (2011), Estimation of the vibration decrement of an offshore wind turbine support structure caused by its interaction with soil, *in* 'Proceedings of the EWEA Offshore 2011 Conference, Amsterdam, The Netherlands, 29 November-1 December 2011', European Wind Energy Association.

Det Norske Veritas (2014), *Design of offshore wind turbine structures - Offshore Standard DNV-OS-J101*, DNV GL AS.

Doherty, P. and Gavin, K. (2011), 'Laterally loaded monopile design for offshore wind farms', *Proceedings of the Institution of Civil Engineers* **165**(EN1), 7–17.

Gazetas, G. (1991), Foundation vibrations, *in* 'Foundation engineering handbook', Springer, pp. 553–593.

Grimstad, G., Andresen, L. and Jostad, H. P. (2012), 'Ngiadp: Anisotropic shear strength model for clay', *International Journal for Numerical and Analytical Methods in Geomechanics* **36**(4), 483–497.

Grimstad, G., Rønningen, J. and Nøst, H. (2014), Use of iwan models for modelling anisotropic and cyclic behavior of clays, *in* 'Numerical Methods in Geotechnical Engineering', pp. 49–54.

Hald, T., Mørch, C., Jensen, L., Bakmar, C. and Ahle, K. (2009), Revisiting monopile design using py curves. results from full scale measurements on horns rev, *in* 'Proceedings of European Offshore Wind 2009 Conference'.

Hamre, L., Khankandi, S. F., Strm, P. and Athanasiu, C. (2010), Lateral behaviour of large diameter monopiles at sheringham shoal wind farm, *in* 'Proceedings of the 2nd International Symposium on Frontiers in Offshore Geotechnics', pp. 575–580.

Hededal, O. and Klinkvort, R. T. (2010), A new elasto-plastic spring element for cyclic loading of piles using the py curve concept, *in* 'Numerical Methods in Geotechnical Engineering', pp. 883–888.

Houlsby, G. and Cassidy, M. (2002), 'A plasticity model for the behaviour of footings on sand under combined loading', *Géotechnique* **52**(2), 117–129.

Iwan, W. D. (1967), 'On a class of models for the yielding behavior of continuous and composite systems', *Journal of Applied Mechanics* **34**(3), 612–617.

Kallehave, D., Byrne, B. W., Thilsted, C. L. and Mikkelsen, K. K. (2015), 'Optimization of monopiles for offshore wind turbines', *Philosophical Transactions of the Royal Society of London A: Mathematical, Physical and Engineering Sciences* **373**(2035), 20140100.

Kallehave, D., Thilsted, C. L. and Troya, A. (2015), Observed variations of monopile foundation stiffness, *in* 'Frontiers in Offshore Geotechnics III', pp. 557–562.

Kaynia, A. and Andersen, K. (2015), Development of nonlinear foundation springs for dynamic analysis of platforms, *in* 'Frontiers in Offshore Geotechnics III', pp. 1067–1072.

Kaynia, A. and Kausel, E. (1982), Dynamic behavior of pile groups, *in* '2nd Int. Conf. on Numerical Methods in Offshore Piling, Austin, Texas', pp. 509–532.

Koiter, W. T. (1953), 'Stress-strain relations, uniqueness and variational theorems for elastic-plastic materials with a singular yield surface', *Quarterly of applied mathematics* **11**(3), 350–354.

Krathe, V. and Kaynia, A. (2017), 'Implementation of a non-linear foundation model for soil-structure interaction analysis of offshore wind turbines in fast', *Wind Energy* **20**(4), 695–712.

Le, T. M. H., Eiksund, G. R., Strøm, P. J. and Saue, M. (2014), 'Geological and geotechnical characterisation for offshore wind turbine foundations: A case study of the sheringham shoal wind farm', *Engineering Geology* **177**, 40–53.

Lesny, K. (2010), *Foundations for offshore wind turbines: tools for planning and design*, VGE Verlag GmbH.

Li, Z., Kotronis, P. and Escoffier, S. (2014), 'Numerical study of the 3D failure envelope of a single pile in sand', *Computers and Geotechnics* **62**, 11–26.

Li, Z., Kotronis, P., Escoffier, S. and Tamagnini, C. (2016), 'A hypoplastic macroelement for single vertical piles in sand subject to three-dimensional loading conditions', *Acta Geotechnica* **11**(2), 373–390.

Masing, G. (1926), Eigenspannungen und verfestigung beim messing, *in* 'Proceedings of the 2nd International Congress of Applied Mechanics', pp. 332–5.

Montáns, F. J. and Caminero, M. A. (2007), 'On the consistency of nested surfaces models and their kinematic hardening rules', *International journal of solids and structures* **44**(14), 5027–5042.

Mrôz, Z. (1967), 'On the description of anisotropic workhardening', *Journal of the Mechanics and Physics of Solids* **15**(3), 163–175.

Nygaard, T. A., De Vaal, J., Pierella, F., Oggiano, L. and Stenbro, R. (2016), 'Development, verification and validation of 3Dfloat; aero-servo-hydro-elastic computations of offshore structures', *Energy Procedia* **94**, 425–433.

Page, A. M., Skau, K. S., Jostad, H. P. and Eiksund, G. R. (2017), 'A new foundation model for integrated analyses of monopile-based offshore wind turbines', *Energy Procedia* **Under review**.

Powell, J. and Butcher, A. (2003), 'Characterisation of a glacial clay till at cowden, humberside', *Characterization and engineering properties of natural soils* **2**, 983–1020.

Prager, W. (1955), 'The theory of plasticity: a survey of recent achievements', *Proceedings of the Institution of Mechanical Engineers* **169**(1), 41–57.

Puzrin, A. M. and Houlsby, G. T. (2001), 'On the non-intersection dilemma in multiple surface plasticity', *Géotechnique* **51**(4), 369–372.

Randolph, M. F. (1981), 'The response of flexible piles to lateral loading', *Géotechnique* **31**(2), 247–259.

Shadlou, M. and Bhattacharya, S. (2014), 'Dynamic stiffness of pile in a layered elastic continuum', *Geotechnique* **64**(4), 303.

Shadlou, M. and Bhattacharya, S. (2016), 'Dynamic stiffness of monopiles supporting offshore wind turbine generators', *Soil Dynamics and Earthquake Engineering* **88**, 15–32.

Shirzadeh, R., Devriendt, C., Bidakhvidi, M. A. and Guillaume, P. (2013), 'Experimental and computational damping estimation of an offshore wind turbine on a monopile foundation', *Journal of Wind Engineering and Industrial Aerodynamics* **120**, 96–106.

Skau, K. S., Grimstad, G., Page, A. M., Eiksund, G. R. and Jostad, H. P. (2017), 'A macro-element for integrated time domain analyses representing bucket foundations for offshore wind turbines', *Under review in Marine Structures* .

Skau, K. S. and Jostad, H. P. (2014), Application of the NGI-procedure for design of bucket foundations for offshore wind turbines.

Tarp-Johansen, N. J., Andersen, L., Christensen, E. D., Mørch, C., Frandsen, S. and Kallesøe, B. (2009), Comparing sources of damping of cross-wind motion, *in* 'The European Offshore Wind Conference & Exhibition', The European Wind Energy Association.

Tian, Y. and Cassidy, M. J. (2008), 'Modeling of pipesoil interaction and its application in numerical simulation', *International Journal of Geomechanics* **8**(4), 213–229.

Tistel, J., Grimstad, G. and Eiksund, G. (2017), 'A macro model for shallow foundations on granular soils describing non-linear foundation behavior', *Computers & Structures* .

Vorpahl, F., Schwarze, H., Fischer, T., Seidel, M. and Jonkman, J. (2013), 'Offshore wind turbine environment, loads, simulation, and design', *Wiley Interdisciplinary Reviews: Energy and Environment* **2**(5), 548–570.

Wind Europe (2018), 'The european offshore wind industry. key trends and statistics 2017', *Wind Europe: Brussels, Belgium* p. 37.

Zaaijer, M. B. (2006), 'Foundation modelling to assess dynamic behaviour of offshore wind turbines', *Applied Ocean Research* **28**(1), 45–57.

Zdravković, L., Taborda, D., Potts, D., Jardine, R., Sideri, M., Schroeder, F., Byrne, B., McAdam, R., Burd, H., Houlsby, G. et al. (2015), Numerical modelling of large diameter piles under lateral loading for offshore wind applications, *in* '3rd International Symposium on Frontiers in Offshore Geotechnics (ISFOG 2015), Oslo, Norway, June'.

Ziegler, H. (1959), 'A modification of Prager's hardening rule', *Quarterly of Applied mathematics* **17**(1), 55–65.